Direct linearly polarized electroluminescence from perovskite nanoplatelet superlattices

Junzhi Ye [1,2], Aobo Ren [3,4], Linjie Dai [1] ✉, Tomi K. Baikie [1], Renjun Guo [5], Debapriya Pal [6], Sebastian Gorgon [1], Julian E. Heger [5], Junyang Huang[1], Yuqi Sun [1], Rakesh Arul [1], Gianluca Grimaldi[6], Kaiwen Zhang[7], Javad Shamsi [1], Yi-Teng Huang [1], Hao Wang [8], Jiang Wu [4], A. Femius Koenderink [6], Laura Torrente Murciano[7], Matthias Schwartzkopf[9], Stephen V. Roth[9,10], Peter Müller-Buschbaum [5,11], Jeremy J. Baumberg [1], Samuel D. Stranks [1,7], Neil C. Greenham [1], Lakshminarayana Polavarapu [12], Wei Zhang [3], Akshay Rao [1] ✉ & Robert L. Z. Hoye [2,13] ✉

Polarized light is critical for a wide range of applications, but is usually generated by filtering unpolarized light, which leads to substantial energy losses and requires additional optics. Here we demonstrate the direct emission of linearly polarized light from light-emitting diodes made of $CsPbI_3$ perovskite nanoplatelet superlattices. The use of solvents with different vapour pressures enables the self-assembly of the nanoplatelets with fine control over their orientation (either face-up or edge-up) and therefore their transition dipole moment. As a result of the highly uniform alignment of the nanoplatelets, as well as their strong quantum and dielectric confinement, large exciton fine-structure splitting is achieved at the film level, leading to pure red light-emitting diodes with linearly polarized electroluminescence exhibiting a high degree of polarization of 74.4% without any photonic structures. This work demonstrates the potential of perovskite nanoplatelets as a promising source of linearly polarized light, opening up the development of next-generation three-dimensional displays and optical communications from a highly versatile, solution-processable system.

Linearly polarized light is essential for numerous applications, including radiometric analysis, bio-imaging, counterfeit detection, liquid crystal displays and emerging three-dimensional display technologies[1–7]. Conventionally, linear polarization is obtained by passing unpolarized light through a linear polarizer, which is typically constructed from highly oriented long-chain molecules or wire grids with photonic structures, reducing the intensity of light by a factor of two or more[1,7]. Organic molecules with aligned transition dipole moments (TDMs) can enable light-emitting diodes (LEDs) with linearly polarized electroluminescence (EL; see Supplementary Table 1 for a comparison of

reported materials), but the degree of polarization (DOP) achieved until now has only been below 40%[8–10]. Photonic structures such as silver nanogratings are generally needed to generate higher DOPs (see Supplementary Table 1)[11]. On the other hand, individual single particles of anisotropic inorganic nanostructures (for example, cadmium selenide nanorods or indium phosphide nanowires) can achieve linearly polarized photoluminescence (PL) with DOPs exceeding 70% (see Supplementary Table 1)[1,2,12–20]. However, the DOP values substantially decrease when integrating single particles together to form nanoparticle films without using patterned photonic substrates because the nanoparticles would then have a random orientation, which limits the ability to translate the polarized emission from single particles to the device level[1,17,21]. Approaches are therefore needed to finely control the orientation of the anisotropic nanostructures to achieve high DOPs in films and devices.

Colloidal perovskite nanocrystals are a promising emerging class of light-emitting materials for display applications[22]. Importantly, it has been shown that perovskite nanocrystals can self-assemble[23,24], and can be passivated using a wide variety of approaches, enabling high photoluminescence quantum yields (PLQYs) that reach up to unity[25–27]. Halide perovskites can also be fabricated as anisotropic nanostructures, such as nanoplatelets (NPLs) and nanowires, which have been reported to yield high DOPs in PL[28–30], and are therefore promising for generating linearly polarized light. Becker et al. found that caesium lead halide nanocrystals have an exciton fine structure with distinct bright triplet states, which could deliver strong linearly polarized emission[30,31]. Seminal works on controlling the TDM alignment in weakly confined $CsPbBr_3$ NPLs (9 ± 2 nm thickness, >10 monolayers) have recently appeared[32,33], but, to the best of our knowledge, there are no reports on the orientation-controlled self-assembly of strongly confined perovskite NPLs (that is, nanocrystals with thicknesses below the Bohr diameter), and no demonstration of direct emission of highly linearly polarized EL from halide perovskite LEDs.

In this work we overcome these pressing challenges to achieve linearly polarized EL directly from perovskite LEDs, which we demonstrate with colour-pure $CsPbI_3$ NPLs. To do this, we focus on addressing four critical factors. The first is to devise a synthesis route to achieve $CsPbI_3$ NPLs with a high degree of uniformity (which is necessary to achieve colour-pure emission) and strong quantum confinement (which is necessary to achieve exciton fine-structure splitting (FSS) and polarized emission). The second is to self-assemble these $CsPbI_3$ NPLs with aligned TDMs. The third is to ensure that the materials have exciton-dominated radiative recombination, and minimize the influence of surface defects on non-radiative recombination. The final factor is to achieve a sufficiently large exciton FSS to obtain emission primarily from a polarized non-degenerate state. This requires not only strong quantum confinement, but also dielectric confinement in a cubic lattice, and is one of the most important factors to achieve high DOPs. In this work we address these four factors and achieve pure red $CsPbI_3$ LEDs with a maximum EL DOP of 74.4%, which, to our knowledge, is the highest EL DOP for any organic or inorganic emitter reported thus far (Supplementary Table 1). These LEDs were based on edge-up NPLs, which exhibited an external quantum efficiency (EQE) of 2%. We achieve higher EQEs of 2.8% in this work through face-down NPLs, due to higher outcoupling in the normal direction to the substrate. An EQE of 2.8%, to our knowledge, exceeds the previously reported performance of strongly confined perovskite NPL emitters (Supplementary Fig. 15). This work also provides a demonstration of pure-red EL from inorganic perovskite NPL LEDs.

Results

Uniform $CsPbI_3$ NPLs with colour-pure luminescence

$CsPbI_3$ NPLs were synthesized by the spontaneous crystallization method using a non-polar toluene solvent for PbI_2 precursors and oleic acid for caesium acetate precursors (Methods)[34]. The PL spectra and transmission electron microscopy (TEM) images of the synthesized

NPLs are given in Fig. 1 and Supplementary Figs. 1–4. Previously reported $CsPbI_3$ NPLs in solution had a shoulder in the PL spectra[34]. We addressed this limitation by replacing the caesium carbonate precursor with caesium acetate, lowering the reaction temperature using an ice bath, and reducing the quantity of caesium acetate used for synthesizing the NPLs (see Supplementary Fig. 5a–c, with a detailed discussion in Supplementary Note 2). The size distribution of the optimized NPLs was analysed via TEM, showing that the NPLs have lengths of 22 ± 2 nm, widths of 22 ± 3 nm and thicknesses of 2.6 ± 0.5 nm (Supplementary Fig. 5d). The thicknesses of the NPLs were much smaller than the Bohr diameter of $CsPbI_3$ (~12 nm)[35], and therefore a strong excitonic peak was observed in the absorption spectra of the NPLs in colloidal solution (Fig. 1b–d). The centre of the PL peak from the NPLs in colloidal solution was at approximately 609 nm (three monolayer NPLs; see spectra in Fig. 1b–d), which is blue-shifted compared with weakly confined $CsPbI_3$ nanocrystals (emitting at ~685 nm wavelength).

Self-assembling $CsPbI_3$ NPLs

We developed a strategy for controlling the orientation of NPLs, which is based on their self-assembly at the solid–air interface following the controlled evaporation of solvents with different vapour pressures[36]. After centrifuging the crude solution at 22,769 relative centrifugal force (g) (14,000 r.p.m.) for 10 min, the precipitated NPLs were dispersed in solvents with different boiling points (bp) and vapour pressures (p_v): hexane (bp = 69 °C, p_v = 20.49 kPa), cyclohexane (bp = 80.75 °C, p_v = 13.01 kPa) and heptane (bp = 98.42 °C, p_v = 6.08 kPa). The solvents do not alter the NPL dimensions, thus maintaining their absorption and PL profiles in solution (Fig. 1b–d). The use of solvents with different boiling points and vapour pressures changes the evaporation rate of the solvents during spin-coating. As a result, the NPLs can be kinetically trapped on the substrate to form films with different orientations. For a slowly evaporating solvent such as heptane, the NPLs adopted a face-down orientation (Fig. 1a,b, inset). By contrast, using a fast-evaporating solvent such as hexane resulted in an edge-up orientation (Fig. 1a,d, inset). Further TEM images with smaller magnifications showing NPLs with different orientations can be found in Supplementary Figs. 1–4.

The change in NPL orientation was corroborated by grazing-incidence wide-angle X-ray scattering (GIWAXS) measurements (Fig. 1e–g). Films with face-down NPLs (Fig. 1e) showed strongly observable peaks associated with (100), (101) and (102) planes (highlighted by the orange boxes from bottom to top, respectively), which became weaker and non-existent in the mixed (Fig. 1f) and edge-up (Fig. 1g) films, respectively[37]. Furthermore, the spread in the scattering of X-rays perpendicular to the diffraction rings in Fig. 1e confirms the layer-by-layer stacking of NPLs in the face-down orientation. Vertical stacking of face-down NPLs resulted in more repetitive planes than edge-up NPLs, leading to stronger diffraction from these periodic planes; please refer to the intensity difference of the fringe inside the orange box for Fig. 1e,g (ref. 37).

Analysis of the line cuts from the GIWAXS data reveals that the high degree of NPL orientation is related to the formation of superlattices during film formation. A schematic of a NPL superlattice is shown in Fig. 2a, depicting face-down NPLs stacked vertically and separated by organic ligands. The regular variation in electron density between the inorganic sub-lattice (high electron density) and organic ligands (low electron density) across the cross-section of the superlattice results in peaks in the low-angle scattering region from the GIWAXS scans, indicating the formation of a superlattice (Fig. 2b)[32,37]. The superlattice peak positions are slightly different across the different NPL orientations in films (Fig. 2b and Supplementary Fig. 6a) due to variations in the average inter-nanoplatelet distances[38]. Further evidence for superlattice formation is provided in Supplementary Fig. 6b, which shows satellite peaks for the edge-up film measured from θ–2θ scans in the Bragg–Brentano geometry, which is in agreement with past studies[38,39].
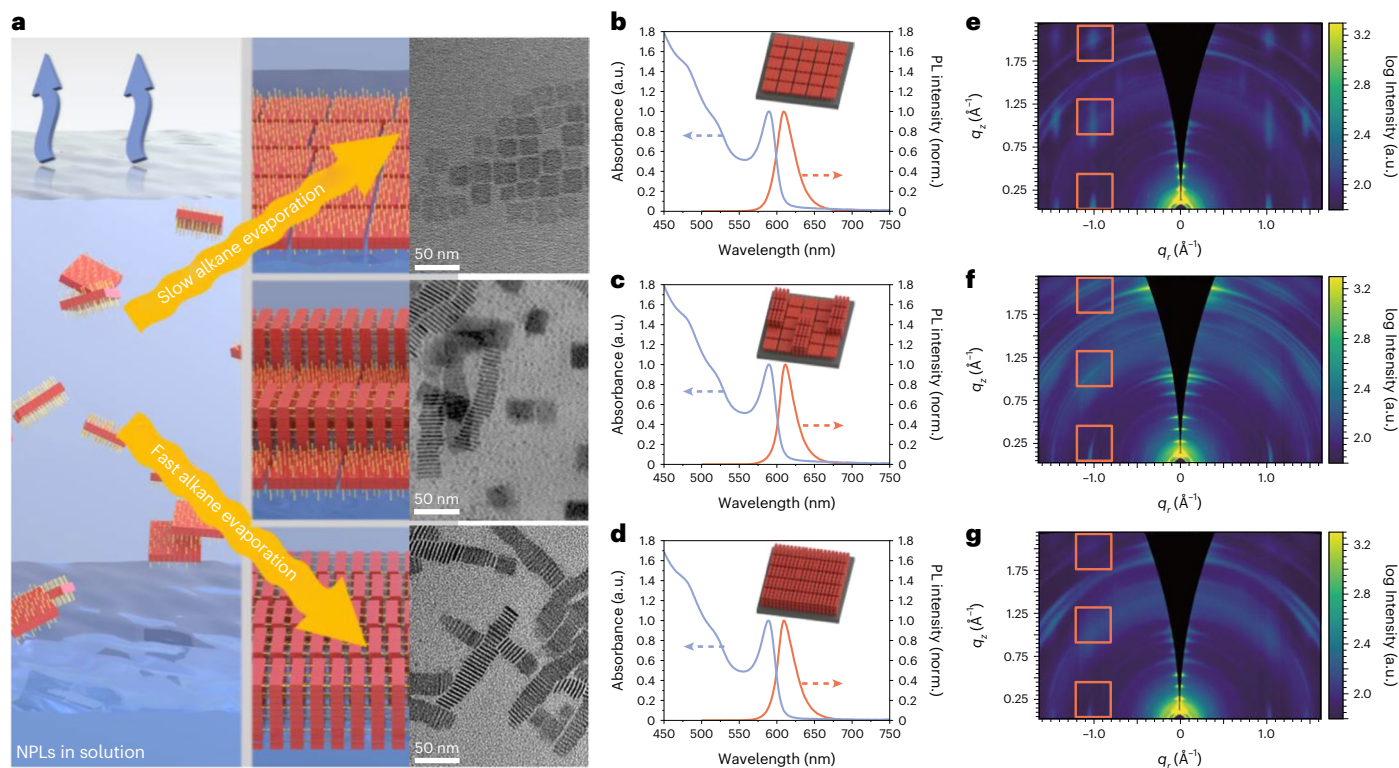
Fig. 1 | Orientation control of self-assembled CsPbI₃ NPLs. a, Schematic illustrating how the orientation of the NPLs could be tuned by adjusting the solvent type and evaporation rate. The insets show TEM images of the face-down (top), mixed (middle) and edge-up (bottom) NPLs drop-cast onto copper TEM grids. **b–d**, Steady-state PL and UV–vis spectra of colloidal solutions of NPLs that were used to form the face-down (**b**), mixed (**c**) and edge-up (**d**) orientation NPL films, respectively. **e–g**, Two-dimensional GIWAXS data of face-down (**e**), mixed (**f**) and edge-up (**g**) NPL films. q_z is the scattering vector component along the surface normal; q_r is the scattering vector component in the sample plane.

Aside from structural evidence, optical analysis also provides strong evidence for self-assembly. Optical simulations of light emission from the films with different transition dipole alignments are shown in Fig. 2c. The labels inset in these contour plots (100% to 0%) represent the percentage of TDMs that are horizontally aligned. These simulations showed that when the dipole was aligned out-of-plane (that is, 0% horizontal TDMs, or perfectly edge-up NPLs), the vertical emission profile mainly came from the out-of-plane dipole (that is, along the confined direction), leading to a lower PL intensity in the normal position compared with the horizontal direction. By contrast, when the NPLs were perfectly face-down (that is, 100% horizontal TDMs), the emission normal to the plane mainly came from the horizontal dipole, leading to stronger PL emission in the normal direction. Changing the NPL orientation from edge-up to face-down would therefore lead to an increase in the normal PL intensity due to an increase in the percentage of horizontal TDMs contributing to this emission[14,32,33,40].

Angle-resolved PL was extracted from *k*-space Fourier microscopy measurements to validate the simulation results (Fig. 2d, blue plots; see Supplementary Fig. 7 and Supplementary Note 4 for experimental details). In the experimental results, 0° is where the collection was perpendicular to the substrate, whereas 90° is collection parallel to the substrate (see Supplementary Fig. 7b,c for the PL spectra at 0° and 89°). By integrating the PL spectra at each collection angle, we found that the edge-up NPL film had higher PL intensities at low collection angles, which then decreased markedly as the collection angle increased. By contrast, the PL intensity for the face-down NPL films remained relatively constant over the range of collection angles (Fig. 2d and Supplementary Fig. 8a). These angle-resolved PL trends agree with the simulation results.

Although we observed a high level of NPL orientation control from the samples drop-cast on TEM grids, as shown in Fig. 1a and

Supplementary Figs. 1–4, we need to determine the uniformity of the orientation of the NPLs deposited into films on device substrates by spin coating. We therefore repeated the optical emission profile measurements by *k*-space Fourier microscopy on five different spots on each film sample. The average emission profile and uncertainties are shown in Supplementary Fig. 8a. The emission profile is consistent within each sample, indicating the orientation to be uniform across the films for both edge-up and face-down NPLs. We also quantified the degree of orientation of the NPLs in films through GIWAXS analysis (Supplementary Note 5)[41,42]. These measurements show that the orientation is not 100% face-down or edge-up (Supplementary Fig. 8b). Rather, the face-down sample has 89.8% of all NPLs across the film face down. This decreased for the mixed sample (79.9% face down), and decreased further to 58.5% for the nominally edge-up film sample. These are consistent with the *k*-space Fourier microscopy measurements, in which the profile for the face-down films matched that of a sample with 80–90% horizontal TDMs (Supplementary Fig. 8c), whereas the edge-up films matched samples with 30–60% horizontal TDMs (Supplementary Fig. 8d). Thus, although there is self-assembly of the NPLs face-down or edge-up, this does not occur over the entire film.

The differences in light outcoupling with NPL orientation indicate that there was a substantial degree of dipole alignment in the films, which is beneficial for generating polarized emission[14]. For example, Achtstein and co-workers illustrated that single-particle NPLs have stronger directional emission with high linear polarization than isotropic spherical quantum dots[40]. Moreover, Gao and co-workers showed that aligning TDMs was critical to achieving polarized PL from MAPbBr₃ polycrystalline films[43]. Thus, the demonstration of fine control over TDM alignment through the formation of self-assembled superlattices is highly promising for achieving polarized light emission.
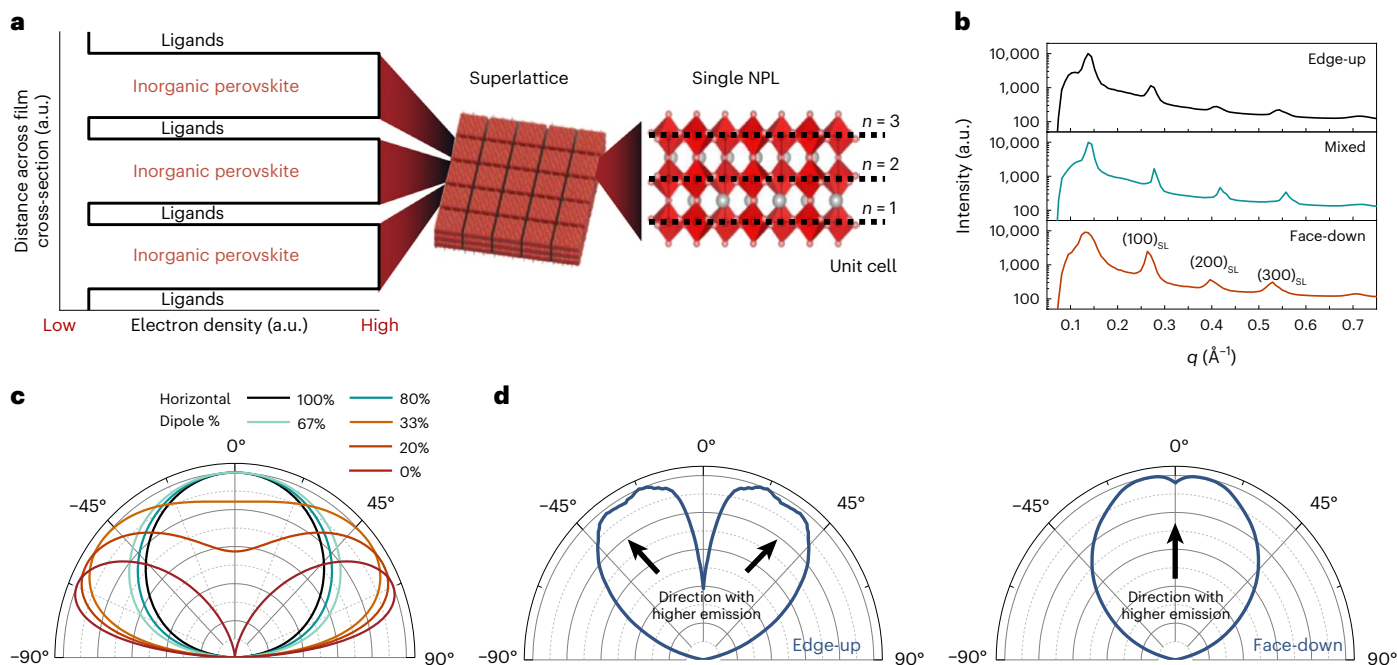
Fig. 2 | Structural and optical characterization of self-assembled NPL films. **a**, Illustration of superlattices formed from the stacking of multiple NPLs, and how the electron density changes between inorganic perovskites and organic ligands. **b**, Radial GIWAXS profiles integrated over all azimuthal angles (pseudo-X-ray diffraction profiles) for different perovskite films in the low-angle region, which demonstrates the formation of a superlattice. q is the absolute value of the scattering vector. SL, superlattice. **c**,**d**, Simulated (**c**) and experimental (**d**) outcoupling from NPL films. The simulations of the outcoupling from the NPL films with different percentages of horizontal TDMs (100% = all NPLs face-down, 0% = all NPLs edge-up) represent different degrees of NPL orientation, and were made assuming that the outcoupling contribution of the TDM in the confined direction is negligible. The simulated radiance was integrated over the azimuthal coordinate as a function of the polar angle (see Methods for details on the simulations). Experimental measurements of the angle-dependent PL obtained from k-space Fourier microscopy are shown in blue; 90° is where the collection was parallel to the substrate, whereas 0° is where the collection was perpendicular to the substrate. Details on data collection and analysis can be found in Supplementary Note 4 and Supplementary Fig. 7.

Reducing non-radiative recombination in CsPbI₃ NPLs

Before developing these self-assembled NPL films into LEDs, we first identified and reduced radiative loss processes at NPL interfaces. We performed X-ray photoelectron spectroscopy (XPS) measurements on the perovskite NPLs, and found the surface to be terminated by Pb and I (Supplementary Fig. 9), with noticeable quantities of metallic Pb (Pb^0). These Pb^0 species—and possibly iodide vacancies—could limit the PLQY of the NPLs in colloidal solution to 48 ± 2% (Fig. 3a). We found that we could improve the PLQY of NPLs in solution to 65 ± 1% by passivating the NPLs with PbI_2 coordinated with oleate and oleylamine ligands (see Supplementary Note 6 for details)[44,45].

As shown in Fig. 3a, the PLQY of the NPLs decreased with an increase in the excitation power density regardless of whether they were passivated. This trend contrasts with weakly confined nanocrystal systems, where the PLQY usually increases with excitation power due to trap filling[46]. The decrease in the PLQY of the NPLs with increasing power density was due to bimolecular exciton–exciton annihilation. Figure 3b demonstrated a linear relationship between the PL intensity and excitation power density, indicating that we have a exciton-dominated recombination system arising from the high exciton binding energies (243 meV; see later in Fig. 5f) as a result of strong dielectric and quantum confinement[35,47].

To understand in greater depth the effect of passivation on exciton kinetics, we measured time-resolved photoluminescence and transient absorption spectroscopy (TAS) of the NPL solutions. The governing equations, and our method for determining the rate constants, are discussed in Supplementary Note 6, with further details in Supplementary Figs. 9–11; the fitting results are shown in Supplementary Table 2. This analysis shows that after PbI_2–ligand passivation, the monomolecular exciton radiative recombination rate (k_{rad}) decreased from 0.008 ns^{-1} (pristine) to 0.004 ns^{-1} (passivated). Meanwhile, the non-radiative monomolecular exciton trapping rate (k_{trap}) decreased from 0.009 ns^{-1} (pristine) to 0.002 ns^{-1} (passivated). Taken together, these results show that the recombination process in the NPLs became increasingly dominated by radiative processes after passivation (consistent with the PLQY measurements), and that the radiative lifetime of the excitons became longer. Furthermore the non-radiative bimolecular exciton–exciton annihilation rate decreased from 0.382 cm^2 s^{-1} (pristine) to 0.282 cm^2 s^{-1} (passivated), as shown in Fig. 3c. When super-positioning the fitted bimolecular exciton–exciton annihilation and monomolecular decay of the passivated sample to the pristine sample in Fig. 3c, there is a clear mismatch of the fitting to the experimental data of the pristine sample, confirming that there were a trap-induced carrier losses at early timescales after excitation for the samples without passivation.

Linearly polarized CsPbI₃ LEDs fulfilling Rec. 2020

Edge-up and face-down NPL films were fabricated into LEDs using the following structure: ITO/PEDOT:PSS/poly-TPD/NPLs/BCP/Ag (Fig. 4b, inset; see Methods for definitions of the terms). The EL spectra at different voltages (3.5–7 V) are shown in Fig. 4a. A red emission with CIE coordinates of (0.661, 0.338) was achieved, which is close to the Rec. 2020 standard for pure red emission (Supplementary Fig. 13a). Unlike the mixed Br–I perovskite systems, the composition purity of CsPbI₃ NPLs in the halide site enabled the devices to avoid halide segregation even at high applied biases (7 V)[46,48]. It was only after increasing the applied bias from 3 V to well above the operational voltage at which the EQE peaked that changes in the EL spectra became noticeable. At 7 V, the CIE coordinates marginally changed from (0.661, 0.338) at 3 V to (0.658, 0.341). This was due to the thermally induced merging of NPLs (Supplementary Fig. 14) resulting from the high current density at this
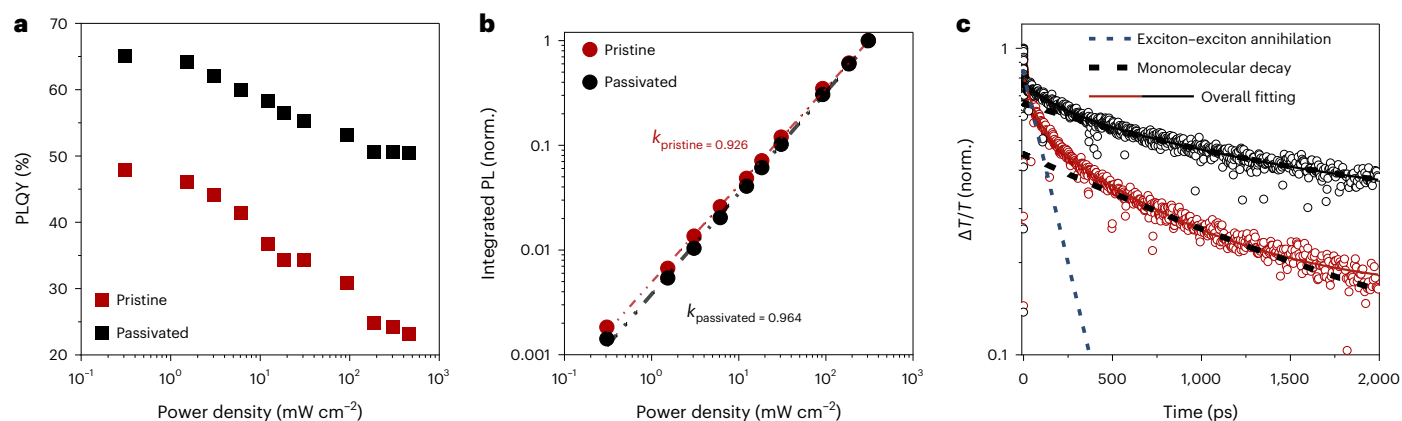
Fig. 3 | Photoluminescence quantum yield of pristine and passivated NPLs.
a, Power density-dependent PLQY (405 nm continuous-wave laser excitation).
b, Power density dependence of the integrated PL peak intensity. $I_{PL} \propto P^k$, where
k is the exponent. When k is close to 1, radiative recombination proceeds in a
monomolecular manner, consistent with the behaviour of excitons. **c**, Short

timescale (0–2 ns) TAS measurements of the ground-state bleach. Excitation was
with a 400 nm wavelength pump laser, 301.5 μJ cm^{-2} pulse^{-1} fluence and a 595 nm
wavelength probe. All samples were in colloidal solution, measured in a cuvette
with a 1-mm-thick cavity.

point, or due to injected charge-carriers increasingly populating the
lower-energy states formed due to the agglomeration of NPLs during
film formation (see 'Discussion'). Through NPL orientation control, we
increased the average EQE of the pristine devices (control) from 1.1%
to 1.2% when changing the NPL orientation from edge-up to face-down
by improving outcoupling (refer back to Fig. 2c,d). After surface pas-
sivation using PbI$_2$–ligand, the median EQE increased from 1.1% to 1.7%
(edge-up NPLs), and from 1.2% to 2.2% (face-down NPLs) (Supplemen-
tary Fig. 13b). Furthermore, passivating the NPLs increased the device
stability (that is, the time it takes for the EL intensity to decrease to half
of the initial peak intensity, t_{50}) from 48 s to 104 s for edge-up NPLs, and
94 s to 147 s for face-down NPLs (Supplementary Fig. 13e). The injected
current was reduced after passivation, especially for the face-down
NPL devices (Supplementary Fig. 13c). The champion NPL device for
edge-up NPLs with PbI$_2$–ligand passivation achieved 2.0% EQE at 4.6 V
(1.85 mA cm^{-2}), with a maximum luminance of 204 cd m^{-2} obtained at
7 V. For face-down NPLs with PbI$_2$–ligand passivation, the champion EQE
achieved was 2.8% at 4 V (1.25 mA cm^{-2}), with a maximum luminance of
408 cd m^{-2} at 7 V (Fig. 4b and Supplementary Fig. 13d). The performance
of these champion face-down and edge-up NPL LEDs is put in context
in Supplementary Fig. 15.

The self-assembly of strongly confined and highly orientated NPLs
led to strongly linearly polarized EL from the LEDs (Fig. 4c–i). To meas-
ure the DOP, circularly polarized light was generated by passing unpo-
larized light from the laser LEDs into a linear polarizer and a waveplate.
The emission of the sample was then passed through a linear polarizer
mounted onto an electrically driven rotation stage and coupled into
a spectrometer (Fig. 4d). The DOP of the EL was recorded in the same
way (Fig. 4g). Both PL and EL showed clear polarized emission relative
to more isotropic emitters, such as weakly confined CsPbI$_3$ nanocube
films and bulk FAPbI$_3$ thin film LEDs.

For the measurements of the DOP in PL (Fig. 4e), we found that the
edge-up configuration (DOP = 12%, PL) had a stronger DOP than the
face-down NPLs (DOP = 4.5%, PL), which is consistent with previous
reports on self-assembled CdSe NPLs[36], as well as theoretical predic-
tions[31] (Fig. 4f). By contrast, the isotropic CsPbI$_3$ nanocrystal control
sample had a low DOP of only 0.4% PL. To measure the DOP for EL, we
accounted for changes in EL intensity over time under operation (Sup-
plementary Fig. 13e,f) to extract only the changes in EL with the angle
of the rotational linear polarizer (Fig. 4g) over several cycles. For the
edge-up LEDs, an EL DOP of 74.4% was achieved (Fig. 4h,i), which is
the highest reported for any organic or inorganic LED without using
photonic gratings (Supplementary Table 1 and Fig. 4c)[17,49,50]. Notably, the

DOP achieved in these film-based LEDs reached the single-particle level
(Fig. 4c). We next examine why the DOP for EL could exceed that for PL.

Discussion

Large exciton FSS enables polarized emission
To understand the origin of the high DOP in the NPL films and devices,
we measured the PL of the face-down and edge-up CsPbI$_3$ NPL films
(Fig. 5a). Linearly polarized PL can arise from the FSS of band-edge
excitons[2,31]. In lead halide perovskites, short- and long-range electron–
hole exchange interactions result in a splitting of the band-edge exci-
tonic states into an optically inactive singlet state with a total angular
momentum of $j = 0$, and three optically active triplet states with $j = 1$
(Fig. 5b)[51]. The triplet states can be split further into two or more ener-
getic states in tetragonal or orthorhombic perovskites through crystal
field effects[51], or in cubic perovskites through strong quantum and
dielectric confinement[31,52–54]. For example, Ghribi et al. showed through
computational analyses that although non-confined cubic perovskites
have degenerate optically active triplets, the state with an out-of-plane
dipole splits away from the two in-plane dipole states as the thickness
of these nanocubes is reduced, and strongly quantum and dielectric
confined NPLs are realized[30] (see Fig. 5b for an illustration of this effect).
Further details on the origin of the splitting in the exciton fine struc-
ture are provided in Supplementary Note 8 and Supplementary Figs.
16 and 17. Others have indeed reported the experimental observation
of FSS from single-particle CsPbBr$_3$ NPLs, that is, the PL spectra split
into multiple peaks (1–3) at cryogenic temperatures[19,55]. However, the
reported FSS was weak and became especially difficult to observe at the
film level when the NPLs or nanocrystals were randomly distributed. In
contrast to these previous experimental results, we were able to
clearly observe PL splitting at 5.2 K at the film level (Fig. 5c,d), which
may have been due to the uniform orientation of the NPLs and the
alignment of their TDMs through self-assembly. We extracted an FSS
energy of 19.77 meV (edge-up) and 11.38 meV (face-down) by fitting the
PL spectra we measured at 5.2 K. These values are much larger than the
FSS energy of the reported isolated cuboidal nanocrystal (~1 meV)[19,30].
As our NPLs are strongly confined in the z-direction, the aspect ratio
(thickness to length/width ratio) is very small (~0.13), and the FSS values
we obtained for such small aspect ratio NPLs match well with predic-
tions from previous theoretical analyses (~20 meV)[31]. If we compare with
weakly confined CsPbI$_3$ nanocrystals or bulk FAPbI$_3$ thin films (Fig. 5e)
with low exciton binding energy (E_b) (Fig. 5f–h) and no self-assembly,
there is no observable exciton fine structure splitting or polarized light
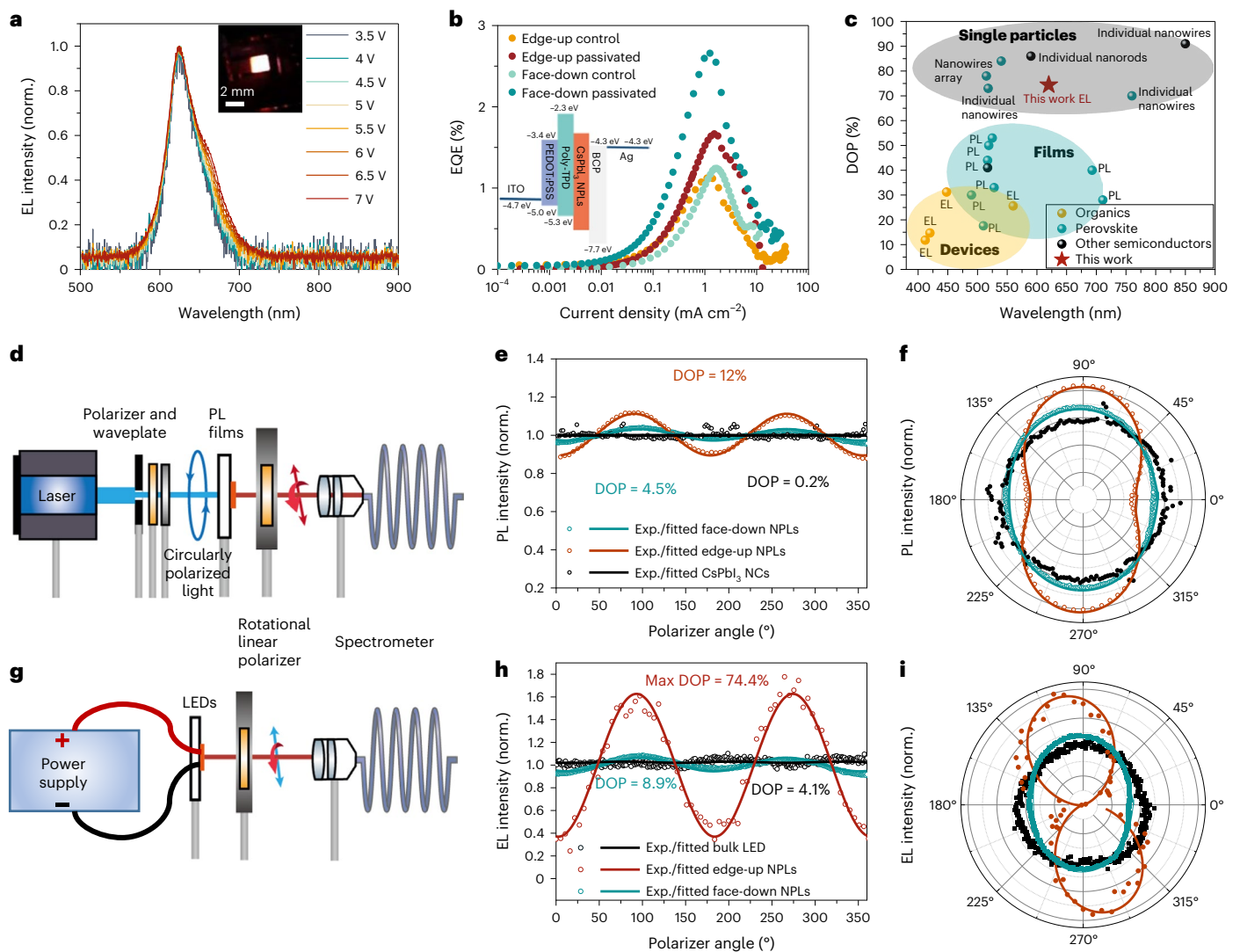emission (refer to end of Supplementary Note 8 for details).

Fig. 4 | Linearly polarized emission from CsPbI₃ NPL films and devices.
a, Electroluminescence spectra of optimized NPL LEDs from 3.5 V to 7 V. The inset shows an LED under operation (pixel area = 0.16 cm²). **b**, Current density against EQE for pristine and passivated edge-up and face-down NPL LEDs. The inset shows the optimized LED device structure: ITO/PEDOT:PSS/poly-TPD/NPLs/BCP/Ag. **c**, Comparison of the DOP of different materials at the single particle, film and device level. **d**, The set-up used to measure the polarized PL. **e**, Polarization dependence of the PL for face-down and edge-up CsPbI₃ NPLs, and bulk FAPbI₃ films at a fixed detection angle of 0° relative to the substrate's normal direction. NCs, nanocubes. **f**, Polar plots of the polarized PL. **g**, Set-up used to measure the polarized EL. **h**, Polarization dependence of the EL for edge-up and face-down CsPbI₃ NPLs, as well as bulk FAPbI₃ LEDs at a fixed detection angle of 0° relative to the substrate's normal direction. **i**, Polar plots of the polarized EL. $DOP = (I_{max} - I_{min})/(I_{max} + I_{min})$.

We were able to fit two peaks to the low-temperature PL spectra of the NPLs (Fig. 5c,d). We attributed the higher-energy PL peak to emission from the out-of-plane dipole (z-direction), and the lower-energy PL peak from the in-plane dipoles (x- and y-directions). The emission from each fine-structure state exhibits single polarization, with the polarization in the x- and y-directions being orthogonal to each other. As we have similar sizes in the x- and y-directions, these two states are essentially degenerate in α-CsPbI₃, and the overall emission would have low or negligible polarization as they cancel each other out to an extent (Supplementary Fig. 16c). The linearly polarized emission from the NPLs would therefore come from the higher energy state (z-direction dipole). From Fig. 5c,d, it can be seen that the edge-up films have stronger emission from these higher-energy states. This was because the collection angle is normal to the film, and the emission in this direction has a strong contribution from the aligned out-of-plane dipole, which has higher energy level in the fine structure. This could explain why the edge-up films have a higher DOP than the face-down NPL films[56]. However, the total DOP and PL splitting should be influenced by

a combination of depolarization within the FSS manifold due to energy transfer[31,57], the detection geometry relative to the crystal plane[55] and the local field effect[58].

Rationalizing the higher DOP in EL than PL
We observed that the EL DOP is much higher than the PL DOP (Fig. 4e,h). To understand the underlying causes, we proposed three possibilities: (1) differences in the areas on the sample contributing to the measured PL and EL, with inhomogeneities in the orientation of the NPLs; (2) differences in the energy state that emission is from in PL versus EL; and (3) changes in exciton FSS under an applied electric field. Detailed discussions on and investigations into these hypotheses can be found in Supplementary Note 9 and Supplementary Figs. 18–21. To summarize, we propose that hypothesis (2) is the most likely, with a small contribution from hypothesis (3). We ruled out hypothesis (1) because the PL and EL spectra—although different to each other—did not change in spectral shape across the entire film (Supplementary Fig. 18). For hypothesis (2), we observed a line shape difference between
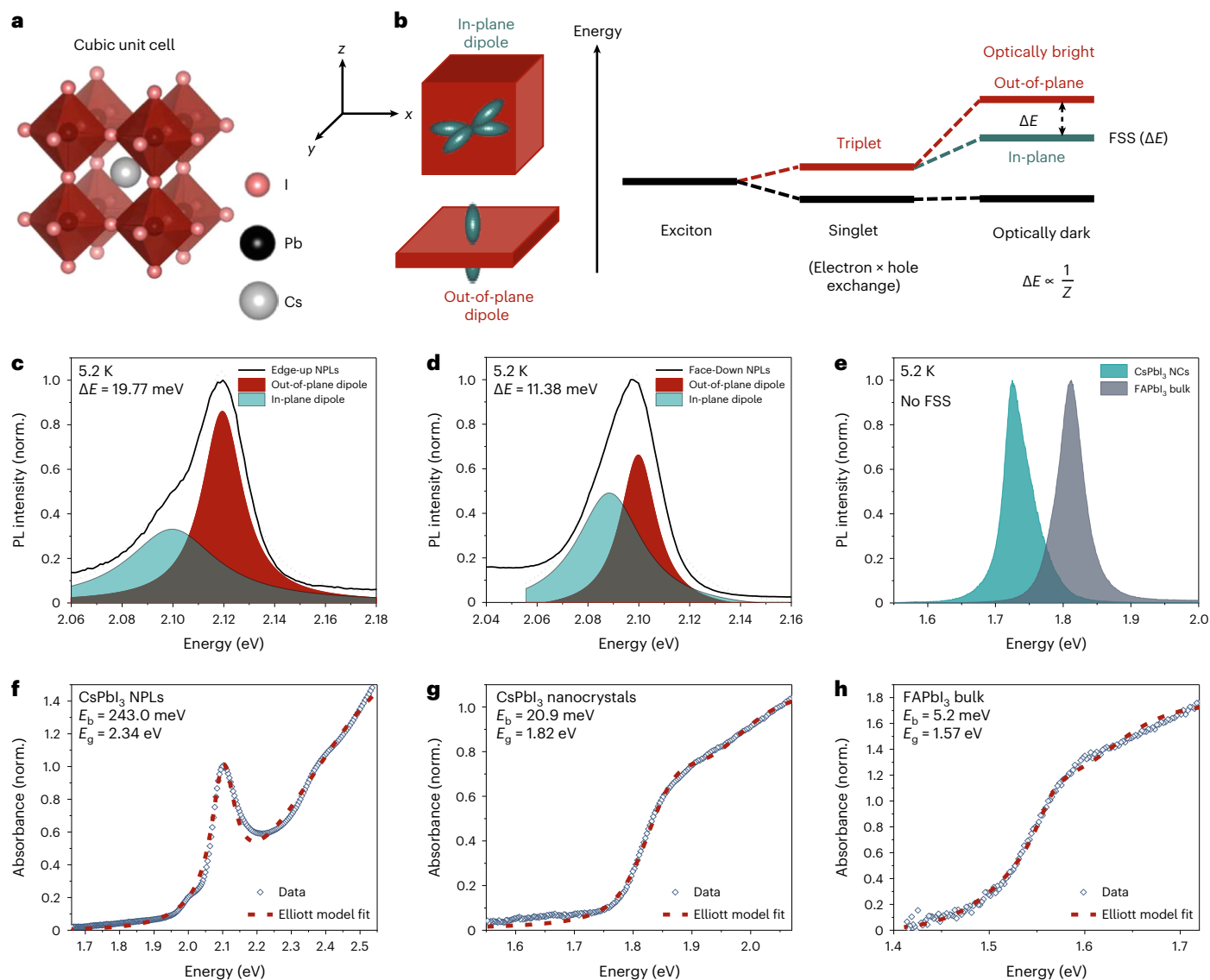
Fig. 5 | Origin of linearly polarized emission. a, Crystal structure of cubic (α-phase) CsPbI$_3$ (Pm$\bar{3}$m). **b**, Schematic to illustrate the influence of quantum and dielectric confinement on exciton fine structure splitting (ΔE). The z-axis is across the thickness of the NPLs. **c,d**, Low-temperature (5.2 K) PL spectra of edge-up (**c**) and face-down (**d**) NPL films. The fitted peaks represent the emission from the exciton fine structure. The detector was held perpendicular to the film. **e**, Low-temperature (5.2 K) PL spectra of CsPbI$_3$ nanocubes and bulk FAPbI$_3$ thin films, from which no excitonic FSS was observed. **f–h**, Elliott model fitting of the absorbance of CsPbI$_3$ NPLs (**f**), CsPbI$_3$ nanocrystals (**g**) and bulk FAPbI$_3$ (**h**) at room temperature to extract E_b. The fitting model is based on the one used in ref. 59, with the fitting code obtained from ref. 60. E_g represents the bandgap.

the PL and EL spectra due to the formation of thicker NPLs during the fabrication of films as a result of agglomeration (Supplementary Figs. 18 and 19). We observed that EL was mainly from the more strongly confined NPLs (Supplementary Fig. 19a), whereas PL was from both the strongly confined NPLs and more weakly confined NPLs/nanocrystals formed during film formation. As discussed above, emission from more strongly confined NPLs would give a higher DOP. For hypothesis (3), we observed that the EL DOP increased with increasing applied voltage (Supplementary Fig. 21a–d), possibly due to a change in exciton FSS with an applied electric field, whereas the PL DOP did not change (Supplementary Fig. 21e–l). We emphasize that other factors are possible. More detailed studies are needed to fully understand the differences in DOP between photo-excitation and electrical injection, for example, into the kinetics of energy transfer within the exciton fine-structure manifolds, as well as analyses of single NPLs devices. We propose that a critical reason for the differences between the EL and PL DOP is the limited transfer of charge-carriers from thinner to thicker NPLs

(Supplementary Fig. 20), but it will be important to investigate this in more detail to fully understand the underlying reasons.

Conclusion

We have demonstrated the direct generation of linearly polarized electroluminescence from halide perovskites through use of strongly confined CsPbI$_3$ NPLs. These nanoplatelet LEDs fulfil Rec. 2020 and have 2.8% EQE (in the face-down orientation), the highest reported thus far for strongly confined NPL LEDs (Supplementary Figs. 13 and 15)[20]. The orientation of the NPLs, and hence the percentage of in-plane/out-of-plane TDMs, can be manipulated via the evaporation rate of the solvent that the colloidal NPLs are dispersed in. Both structural (TEM, GIWAXS) and optical (angular-resolved PL) characterization confirmed our ability to control the orientation of NPL films through self-assembly. Detailed carrier dynamics measurements—using time-resolved photoluminescence and TAS—helped us to develop a passivation process for CsPbI$_3$ NPLs that reduced

both monomolecular trap-assisted-recombination and bimolecular exciton–exciton annihilation. Importantly, we demonstrated a high degree of linear polarization (74.4%) in the EL from pure-red LED devices with edge-up NPLs, which is attributed to three key factors: (1) highly uniform alignment of the NPLs, (2) high PLQYs, such that the emission is strongly governed by the radiative recombination of band-edge excitons and (3) large exciton fine structure splitting due to strong quantum and dielectric confinement, which was preserved at the film-level due to the formation of strongly aligned NPL superlattices. This work opens up a new frontier in enabling applications for displays and optical communications with more efficient linearly polarized LEDs.

Online content

Any methods, additional references, Nature Portfolio reporting summaries, source data, extended data, supplementary information, acknowledgements, peer review information; details of author contributions and competing interests; and statements of data and code availability are available at https://doi.org/10.1038/s41566-024-01398-y.

References

1. Wang, M., Yang, Z. & Zhang, C. Polarized photoluminescence from lead halide perovskites. *Adv. Opt. Mater.* **9**, 2002236 (2021).
2. Ge, Y., Meng, L., Bai, Z. & Zhong, H. Linearly polarized photoluminescence from anisotropic perovskite nanostructures: emerging materials for display technology. *J. Inf. Disp.* **20**, 181–192 (2019).
3. Geng, J. Three-dimensional display technologies. *Adv. Opt. Photon.* **5**, 456–535 (2013).
4. Cunningham, P. D. et al. Assessment of anisotropic semiconductor nanorod and nanoplatelet heterostructures with polarized emission for liquid crystal display technology. *ACS Nano* **10**, 5769–5781 (2016).
5. Wyatt, C. L. in *Radiometric Calibration: Theory and Methods* (ed. Clair L. Wyatt) 151–162 (Academic, 1978).
6. Bloxham, W., Brinks, D., Kheifets, S. & Cohen, A. E. Linearly polarized excitation enhances signals from fluorescent voltage indicators. *Biophys. J.* **120**, 5333–5342 (2021).
7. Srivastava, A. K. et al. Photoaligned nanorod enhancement films with polarized emission for liquid-crystal-display applications. *Adv. Mater.* **29**, 1701091 (2017).
8. Geng, Y., Culligan, S. W., Trajkovska, A., Wallace, J. U. & Chen, S. H. Monodisperse oligofluorenes forming glassy-nematic films for polarized blue emission. *Chem. Mater.* **15**, 542–549 (2003).
9. Culligan, S. W. et al. Strongly polarized and efficient blue organic light-emitting diodes using monodisperse glassy nematic oligo(fluorene)s. *Adv. Mater.* **15**, 1176–1180 (2003).
10. Chen, A. C. A. et al. Organic polarized light-emitting diodes via Förster energy transfer using monodisperse conjugated oligomers. *Adv. Mater.* **16**, 783–788 (2004).
11. Ming Yi, L., Yi Jiun, C., Hoang Yan, L. & Si-Chen, L. in *2012 12th IEEE International Conference on Nanotechnology (IEEE-NANO)* 1–4 (IEEE, 2012).
12. Hu, J. et al. Linearly polarized emission from colloidal semiconductor quantum rods. *Science* **292**, 2060–2063 (2001).
13. Wang, J., Gudiksen, M. S., Duan, X., Cui, Y. & Lieber, C. M. Highly polarized photoluminescence and photodetection from single indium phosphide nanowires. *Science* **293**, 1455–1457 (2001).
14. Jurow, M. J. et al. Manipulating the transition dipole moment of CsPbBr$_3$ perovskite nanocrystals for superior optical properties. *Nano Lett.* **19**, 2489–2496 (2019).
15. Liu, J. et al. Polarized emission from single perovskite FAPbBr$_3$ nanocrystals. *J. Lumin.* **221**, 117032 (2020).
16. Wang, J. et al. Strong polarized photoluminescence CsPbBr$_3$ nanowire composite films for UV spectral conversion polarization photodetector enhancement. *ACS Appl. Mater. Interfaces* **13**, 36147–36156 (2021).
17. Lin, C.-H. et al. Giant optical anisotropy of perovskite nanowire array films. *Adv. Funct. Mater.* **30**, 1909275 (2020).
18. Yang, D. et al. Facet-induced coordination competition for highly ordered CsPbBr$_3$ nanoplatelets with strong polarized emission. *Nano Res.* **15**, 502–509 (2022).
19. Huo, C. et al. Optical spectroscopy of single colloidal CsPbBr$_3$ perovskite nanoplatelets. *Nano Lett.* **20**, 3673–3680 (2020).
20. Otero-Martínez, C. et al. Colloidal metal–halide perovskite nanoplatelets: thickness-controlled synthesis, properties, and application in light-emitting diodes. *Adv. Mater.* **34**, 2107105 (2022).
21. Wei, Y. et al. CsPbBr$_3$ nanowire polarized light-emitting diodes through mechanical rubbing. *Chem. Commun.* **56**, 5413–5416 (2020).
22. Dey, A. et al. State of the art and prospects for halide perovskite nanocrystals. *ACS Nano* **15**, 10775–10981 (2021).
23. Jana, A. et al. Self-assembly of perovskite nanocrystals. *Prog. Mater Sci.* **129**, 100975 (2022).
24. Liu, J., Zheng, X., Mohammed, O. F. & Bakr, O. M. Self-assembly and regrowth of metal halide perovskite nanocrystals for optoelectronic applications. *Acc. Chem. Res.* **55**, 262–274 (2022).
25. Bi, C. et al. Self-assembled perovskite nanowire clusters for high luminance red light-emitting Diodes. *Adv. Funct. Mater.* **30**, 2005990 (2020).
26. Tong, Y. et al. From precursor powders to CsPbX$_3$ perovskite nanowires: one-pot synthesis, growth mechanism, and oriented self-assembly. *Angew. Chem. Int. Ed.* **56**, 13887–13892 (2017).
27. Wu, Y. et al. In situ passivation of PbBr$_6^{4-}$ octahedra toward blue luminescent CsPbBr$_3$ nanoplatelets with near 100% absolute quantum yield. *ACS Energy Lett.* **3**, 2030–2037 (2018).
28. Täuber, D., Dobrovolsky, A., Camacho, R. & Scheblykin, I. G. Exploring the electronic band structure of organometal halide perovskite via photoluminescence anisotropy of individual nanocrystals. *Nano Lett.* **16**, 5087–5094 (2016).
29. Ghoshal, D. et al. Catalyst-free and morphology-controlled growth of 2D perovskite nanowires for polarized light detection. *Adv. Opt. Mater.* **7**, 1900039 (2019).
30. Becker, M. A. et al. Bright triplet excitons in caesium lead halide perovskites. *Nature* **553**, 189–193 (2018).
31. Ghribi, A. et al. Dielectric confinement and exciton fine structure in lead halide perovskite nanoplatelets. *Nanomaterials* **11**, 3054 (2021).
32. Kumar, S. et al. Anisotropic nanocrystal superlattices overcoming intrinsic light outcoupling efficiency limit in perovskite quantum dot light-emitting diodes. *Nat. Commun.* **13**, 2106 (2022).
33. Cui, J. et al. Efficient light-emitting diodes based on oriented perovskite nanoplatelets. *Sci. Adv.* **7**, eabg8458 (2020).
34. Huang, H. et al. Spontaneous crystallization of perovskite nanocrystals in nonpolar organic solvents: a versatile approach for their shape-controlled synthesis. *Angew. Chem. Int. Ed.* **58**, 16558–16562 (2019).
35. Protesescu, L. et al. Nanocrystals of cesium lead halide perovskites (CsPbX$_3$, X = Cl, Br, and I): novel optoelectronic materials showing bright emission with wide color gamut. *Nano Lett.* **15**, 3692–3696 (2015).
36. Momper, R. et al. Kinetic control over self-assembly of semiconductor nanoplatelets. *Nano Lett.* **20**, 4102–4110 (2020).
37. Toso, S. et al. Multilayer diffraction reveals that colloidal superlattices approach the structural perfection of single crystals. *ACS Nano* **15**, 6243–6256 (2021).
38. Toso, S., Baranov, D., Filippi, U., Giannini, C. & Manna, L. Collective diffraction effects in perovskite nanocrystal superlattices. *Acc. Chem. Res.* **56**, 66–76 (2023).

39. Toso, S., Baranov, D., Giannini, C., Marras, S. & Manna, L. Wide-angle X-ray diffraction evidence of structural coherence in CsPbBr$_3$ nanocrystal superlattices. *ACS Mater. Lett.* **1**, 272–276 (2019).

40. Scott, R. et al. Directed emission of CdSe nanoplatelets originating from strongly anisotropic 2D electronic structure. *Nat. Nanotech.* **12**, 1155–1160 (2017).

41. Oesinghaus, L. et al. Toward tailored film morphologies: the origin of crystal orientation in hybrid perovskite thin films. *Adv. Mater. Interfaces* **3**, 1600403 (2016).

42. Zou, Y. et al. Ionic liquids tailoring crystal orientation and electronic properties for stable perovskite solar cells. *Nano Energy* **112**, 108449 (2023).

43. Qin, J. et al. Aligning transition dipole moment toward light amplification and polarized emission in hybrid perovskites. *Adv. Opt. Mater.* **9**, 2100984 (2021).

44. Liang, J. et al. Origins and influences of metallic lead in perovskite solar cells. *Joule* **6**, 816–833 (2022).

45. Hu, J., Kerner, R. A., Pelczer, I., Rand, B. P. & Schwartz, J. Organoammonium-ion-based perovskites can degrade to Pb^0 via amine–Pb(II) coordination. *ACS Energy Lett.* **6**, 2262–2267 (2021).

46. Ye, J. et al. Elucidating the role of antisolvents on the surface chemistry and optoelectronic properties of CsPbBr$_x$I$_{3-x}$ perovskite nanocrystals. *J. Am. Chem. Soc.* **144**, 12102–12115 (2022).

47. Liu, Q. et al. Exciton relaxation dynamics in photo-excited CsPbI$_3$ perovskite nanocrystals. *Sci. Rep.* **6**, 29442 (2016).

48. Hassan, Y. et al. Ligand-engineered bandgap stability in mixed-halide perovskite LEDs. *Nature* **591**, 72–77 (2021).

49. Güner, T. et al. Polarized emission from CsPbBr$_3$ nanowire embedded-electrospun PU fibers. *Nanotechnology* **29**, 135202 (2018).

50. Wang, D. et al. Polarized emission from CsPbX$_3$ perovskite quantum dots. *Nanoscale* **8**, 11565–11570 (2016).

51. Sercel, P. C. et al. Exciton fine structure in perovskite nanocrystals. *Nano Lett.* **19**, 4068–4077 (2019).

52. Han, Y. et al. Lattice distortion inducing exciton splitting and coherent quantum beating in CsPbI$_3$ perovskite quantum dots. *Nat. Mater.* **21**, 1282–1289 https://doi.org/10.1038/s41563-022-01349-4 (2022).

53. Takagahara, T. Effects of dielectric confinement and electron-hole exchange interaction on excitonic states in semiconductor quantum dots. *Phys. Rev. B* **47**, 4569–4584 (1993).

54. Rajadell, F., Climente, J. I. & Planelles, J. Excitons in core-only, core-shell and core-crown CdSe nanoplatelets: interplay between in-plane electron-hole correlation, spatial confinement, and dielectric confinement. *Phys. Rev. B* **96**, 035307 (2017).

55. Schmitz, A. et al. Optical probing of crystal lattice configurations in single CsPbBr$_3$ nanoplatelets. *Nano Lett.* **21**, 9085–9092 (2021).

56. Krajewska, C. J. et al. Controlled assembly and anomalous thermal expansion of ultrathin cesium lead bromide nanoplatelets. *Nano. Lett.* **23**, 2148–2157 (2023).

57. Gramlich, M. et al. Dark and bright excitons in halide perovskite nanoplatelets. *Adv. Sci.* **9**, 2103013 (2022).

58. Rodina, A. V. & Efros, A. L. Effect of dielectric confinement on optical properties of colloidal nanostructures. *J. Exp. Theor. Phys.* **122**, 554–566 (2016).

59. Naeem, A. et al. Giant exciton oscillator strength and radiatively limited dephasing in two-dimensional platelets. *Phys. Rev. B* **91**, 121302 (2015).

60. Hoye, R. L. Z. et al. Identifying and reducing interfacial losses to enhance color-pure electroluminescence in blue-emitting perovskite nanoplatelet light-emitting diodes. *ACS Energy Lett.* **4**, 1181–1188 (2019).

Methods

CsPbI₃ NPL synthesis

Materials. CH₃COOCs (caesium acetate, 99.9% trace metal basis), PbI₂ (lead(II) iodide 99%), oleic acid (technical grade 90%), oleylamine (technical grade 70%), toluene (anhydrous, >99.8%) and heptane (grade ≥ 99.0%; HPLC, GC) were purchased from Sigma-Aldrich. All chemicals were used as received.

Synthesis. The synthesis method was modified from a previously reported method[34]. Caesium oleate precursor was prepared by dissolving 0.5 mmol caesium acetate in 10 ml of oleic acid (concentration = 0.05 mol l⁻¹), stirring at 60 °C for 1 h. PbI₂ precursor solution was prepared by dissolving 0.1 mmol PbI₂ powder (46.1 mg) in a mixture of 100 μl of oleic acid, 100 μl oleylamine and 10 ml toluene (concentration = ~0.01 mol l⁻¹) at 80 °C under continuous stirring. Both precursor solutions were then cooled to room temperature. In a typical NPL synthesis, 10 ml of PbI₂ precursor solution was taken to a glass vial with stir bar; the glass vial was then placed in an ice-water-bath and stirred for 2 min. Finally, 250 μl of caesium oleate was added into 10 ml of PbI₂ precursor (prepared in toluene) solution under vigorous stirring in the ice-water bath. After 2 min of stirring, the solution was poured into a centrifuge tube and centrifuged at 22,769 relative centrifugal force (*g*) for 10 min and the precipitate was redispersed in 2 ml of hexane (edge-up), cyclohexane (mixture of edge-up and face-down) or heptane (face-down).

Light-emitting diode device fabrication and characterization

Device fabrication. Indium tin oxide (ITO)/glass substrates (Colorado Concept Coatings LLC) were cleaned by ultrasonication in acetone and isopropanol for 15 min each, and then dried in the oven. The substrates were subsequently O₂-plasma treated for 10 min at 250 W forward power (0 W reverse power), using a radiofrequency plasma source. For bipolar devices, poly(3,4-ethylene dioxythiophene) polystyrene sulfonate (PEDOT:PSS; Heraeus Clevios P Al.4083) was subsequently deposited at 3,500 r.p.m. for 30 s (1,000 r.p.m. s⁻¹ acceleration) and then annealed at 145 °C for 15 min. Poly(*N*,*N*′-bis(4-butylphenyl)-*N*,*N*′-bis-phenylbenzidine) (poly-TPD; 1-Material) was dissolved in chlorobenzene (anhydrous 99.8%, Sigma-Aldrich) with a concentration of 8 mg ml⁻¹. These polymer layers were spin-cast over the PEDOT:PSS at 2,000 r.p.m. for 30 s inside a nitrogen-filled glovebox and annealed at 120 °C for 10 min. The NPLs were subsequently deposited at 1,500 r.p.m. for 30 s inside an N₂-filled glovebox; 20 nm of 2,9-dimethyl-4,7-diphenyl-1,10-phenanthroline (BCP; Ossila) was thermally evaporated over the NPLs under a base pressure of 1 × 10⁻⁶ mbar, followed by 100 nm Ag. The devices were measured in ambient.

Light-emitting diode device characterization. Current density–voltage characteristics were measured using a Keithley 2400 source-meter unit. The photon flux was measured simultaneously using calibrated silicon photodiodes centred over the LED. The radiance (in W sr⁻¹ m⁻²) of the devices was calculated on the basis of the emission function of the perovskite-polymer bulk heterostructure LED and on the known spectral response of the silicon photodiode; the EQEs were calculated assuming a Lambertian profile. The electroluminescence spectra of the devices were measured using a calibrated iCCD camera system (AndoriStar DH740 CCI-010) connected to a grating spectrometer (Andor SR303i). The accuracy of the spectral data was cross-checked against a Labsphere CDS-610 spectrometer. All devices were characterized at room temperature without encapsulation (see Supplementary Fig. 14 for temperature reached in devices after 30 s operation). The thickness is 18 nm for the face-down NPL film, and 38 nm for the edge-up NPL film, as measured by ellipsometry (Supplementary Fig. 12).

Characterization

Transmission electron microscopy. Transmission electron microscopy samples were prepared by putting a small drop of nanoparticle solution onto the carbon-coated copper grid in a glovebox; TEM images were recorded using a FEI Tecnai F20 (120 kV). A GATAN 648 vacuum transfer holder was used to eliminate the exposure to the ambient atmosphere to avoid modification of the nanoparticles between the glove box and the TEM vacuum.

Ultraviolet–visible absorption spectrophotometry. Spectra were recorded on a Shimadzu ultraviolet–visible–near infrared spectrophotometer (UV-3600Plus). The absorption spectra were measured on nanocrystal thin films, which were prepared by spin-coating the NPL solutions onto pre-cleaned glass substrates at 1,500 r.p.m. for 30 s in air. All glass substrates are cleaned with acetone and isopropanol separately in an ultrasonic bath for 15 min.

Steady-state PL spectra. Steady-state PL spectra were recorded using a Horiba Fluorolog system with an integrating sphere and a monochromatic xenon lamp as the excitation source.

Photoluminescence quantum yield. The PLQY of the perovskite NPL solutions and films was measured using a commercial set-up from Ocean Optics with excitation from a 405 nm wavelength continuous-wave diode laser.

Grazing-incidence wide-angle X-ray scattering. Two-dimensional GIWAXS data were taken at the P03 MiNaXS beamline, PETRA III at DESY in Hamburg[61]. A LAMBDA 9M detector from X-Spectrum was used with a wavelength of 1.05 Å. The INSIGHT[62] software was used to process the 2D data. This includes transformation to q-space, flatfield correction, masking, intensity corrections for detector absorption, solid angle, photon polarization and path attenuation and obtaining pseudo-XRD cuts. The sample-to-detector distance were calibrated by AgBeh and CeO₂ for GISAXS and GIWAXS separately, and the samples were aligned with the GISAXS mode.

Time-correlated single photon counting measurements. The spin-coated nanoplatelet thin films (edge-up and face-down with passivation and without passivation) were photoexcited using a 407 nm pulsed laser with a pulse width <200 ps, at a repetition rate of 40 MHz. Photons emitted from the sample were collected by a silicon-based single-photon avalanche photodiode. The instrument response function has a lifetime of ~0.2 ns. A 420 nm long-pass filter was used to screen-out any scattered laser signal in the optical path.

Transient absorption spectroscopy. The output of a Ti:sapphire amplifier system (Spectra Physics Solstice Ace) operating at 1 kHz and generating ~100 fs pulses (fundamental, 800 nm) was split into pump and probe pulses. The 400 nm pump pulses were created by sending the 800 nm fundamental beam of the Solstice Ace through a second harmonic generating beta barium borate crystal (Eksma Optics). The pump was blocked by a chopper wheel rotating at 500 Hz. The broadband probe (330–700 nm) was generated by focusing the 800 nm fundamental beam onto a CaF₂ crystal (Eksma Optics, 5 mm) connected to a digital motion controller (Mercury C-863 DC Motor Controller). The pump–probe delay (100 fs to 2 ns) was controlled by a mechanical delay stage (Thorlabs DDS300-E/M). The transmitted pulses are collected with a monochrome line scan camera (JAI SW-4000M-PMCL, spectrograph: Andor Shamrock SR-163). The spectrum was taken with solution samples inside a 1 mm thick cuvette. The thin film samples are NPLs spin coated on ITO glass substrates.

X-ray photoelectron spectroscopy. X-ray photoelectron spectroscopy data were acquired using a Kratos Axis SUPRA using monochromatic Al Kα (1486.69 eV) X-rays at 12 mA emission and 15 kV HT (180 W), with an analysis area of 700 × 300 μm². The instrument was calibrated to the gold metal gold 4*f* core level (83.95 eV) and dispersion adjusted give a binding energy of 932.6 eV for the copper 2*p*₃/₂ line of metallic

copper. The silver $3d_{5/2}$ line full-width at half-maximum at 10 eV pass energy was 0.544 eV. Source resolution for monochromatic silver K_α X-rays is ~0.3 eV. The instrumental resolution was determined to be 0.29 eV at 10 eV pass energy using the Fermi edge of the valence band for metallic silver. Resolution with charge compensation system on <1.33 eV FWHM on PTFE. High-resolution spectra were obtained using a pass energy of 20 eV, step size of 0.1 eV and sweep time of 60 s, resulting in a line width of 0.696 eV for gold $4f_{7/2}$. Survey spectra were obtained using a pass energy of 160 eV. Charge neutralization was achieved using an electron flood gun with filament current = 0.38 A, charge balance = 2 V, filament bias = 4.2 V. Successful neutralization was adjudged by analysing the carbon $1s$ region wherein a sharp peak with no lower binding energy structure was obtained. The spectra were charge corrected to the main line of the carbon 1 s spectrum (adventitious carbon) set to 284.8 eV. All data was recorded at a base pressure of below 9×10^{-9} Torr and at room temperature (294 K). Data were analysed using the software CasaXPS v.2.3.19PR1.0.

Polarization-dependent photoluminescence and electroluminescence measurement. For PL polarization measurement, a 405 nm laser diode was used to excite the film through the glass side (as shown in Fig. 4d). Circularly polarized light was generated by passing through the 405 nm laser light into a linear polarizer-quarter waveplate optic (CP1L405, Thorlabs). After excitation of the film, one the collection beam pass, a 405 nm filter and a linear polarizer (WP50L-VIS, purchased from Thorlabs) was placed before photodetector and spectrometer. During the PL polarization measurement, linear polarizer was rotated via a motorized rotation mount (K10CR1/M, purchased from Thorlabs) with a step of 50 and step interval of 10 s for spectrum collection. For the EL polarization measurement, the LEDs are powered by a Keithley power supply at a constant voltage of 5 V, then the linear polarizer is rotated the same way as measuring the PL.

Optical simulation

The optical simulation for Fig. 2c was performed based on the Green function, which is described below:

The electric field generated at position r, due to a dipole source at r_0, is calculated via the electric Green function $G(r,r_0)$ in free space. In the case of a dipole placed within a multilayer structure, Green's function for the system can be separated into two parts: the free space part and the reflected part. The reflected part contains the $k_{||}$-dependent Fresnel reflection coefficients for different polarizations. We use this system Green's function to estimate the electric field from a dipole source inside the multilayer structure to infinite half spaces (super/substrate). We use the far field approximation to Green's function to obtain the radiation patterns, which involves a transformation from Cartesian to spherical coordinates. Thus, using the asymptotic electric field, we calculate the radiated power per unit solid angle by integrating the time-averaged Poynting vector, which gives the radiation pattern.

$$E(r) = \omega^2 \mu_0 \, G(r,r_0)\,\mu \tag{1}$$

where μ_0 is the vacuum permeability. The thickness of the active layer and the corresponding NPL dimensions—as measured by ellipsometry—reveal that the edge-up and face-down NPL films have a thickness of 38 nm and 17 nm, respectively; we assume that the total thickness is made of two and six dipole sources stacked vertically for edge-up and face-down films, respectively. The radiation patterns for each dipole source, for a given orientation, are then added up incoherently to find the resulting radiation pattern for the whole layer (the results are shown in Fig. 2c).

Data availability

The raw data for this paper and Supplementary Information have been deposited to the Oxford Research Data Archive, with the link https://doi.org/10.5287/ora-2zq2ywbjg.

References

61. Buffet, A. et al. P03, the microfocus and nanofocus X-ray scattering (MiNaXS) beamline of the PETRA III storage ring: the microfocus endstation. *J. Synchrotron Radiat.* **19**, 647–653 (2012).
62. Reus, M. A. et al. Time-resolved orientation and phase analysis of lead halide perovskite film annealing probed by in situ GIWAXS. *Adv. Opt. Mater.* **10**, 2102722 (2022).

Author contributions

J.Y. and R.L.Z.H. conceived of the project. J.Y. synthesized the materials and films. J.S. and L.P. contributed toward materials synthesis optimization. L.D. and J.Y. conceived the idea for orientation control of NPLs and helped design the method by which GIWAXS measurements were performed. L.D. and K.Z. performed TEM under supervision from S.D.S. and L.T.M. J.Y. and Y.-T.H. performed TAS and transient

Competing interests

Additional information